

Efficient metallic spintronic emitters of ultrabroadband terahertz radiation

T. Seifert¹, S. Jaiswal^{2,3}, U. Martens⁴, J. Hannegan⁵, L. Braun¹, P. Maldonado⁶, F. Freimuth⁷, A. Kronenberg², J. Henrizi², I. Radu⁸, E. Beaupaire⁹, Y. Mokrousov⁷, P. M. Oppeneer⁶, M. Jourdan², G. Jakob², D. Turchinovich¹⁰, L. M. Hayden⁵, M. Wolf¹, M. Münzenberg⁴, M. Kläui² and T. Kampfrath^{1*}

Terahertz electromagnetic radiation is extremely useful for numerous applications, including imaging and spectroscopy. It is thus highly desirable to have an efficient table-top emitter covering the 1–30 THz window that is driven by a low-cost, low-power femtosecond laser oscillator. So far, all solid-state emitters solely exploit physics related to the electron charge and deliver emission spectra with substantial gaps. Here, we take advantage of the electron spin to realize a conceptually new terahertz source that relies on three tailored fundamental spintronic and photonic phenomena in magnetic metal multilayers: ultrafast photoinduced spin currents, the inverse spin-Hall effect and a broadband Fabry-Pérot resonance. Guided by an analytical model, this spintronic route offers unique possibilities for systematic optimization. We find that a 5.8-nm-thick W/CoFeB/Pt trilayer generates ultrashort pulses fully covering the 1–30 THz range. Our novel source outperforms laser-oscillator-driven emitters such as ZnTe(110) crystals in terms of bandwidth, terahertz field amplitude, flexibility, scalability and cost.

The terahertz window, loosely defined as the frequency range 0.3–30 THz in the electromagnetic spectrum, is located between the realms of electronics and optics^{1,2}. As this region coincides with many fundamental resonances of materials, terahertz radiation enables very selective spectroscopic insights into all phases of matter with high temporal^{3,4} and spatial^{5–8} resolution. Consequently, numerous applications in basic research^{3,4}, imaging⁵ and quality control⁸ have emerged.

To fully exploit the potential of terahertz radiation, energy-efficient and low-cost sources of ultrashort terahertz pulses are required. Most broadband table-top emitters are driven by femtosecond laser pulses that generate the required terahertz charge current by appropriately mixing the various optical frequencies^{9,10}. Sources made from solids usually consist of semiconducting or insulating structures with naturally or artificially broken inversion symmetry. When the incident photon energy is below the semiconductor bandgap, optical rectification causes a charge displacement that follows the intensity envelope of the incident pump pulse^{9–17}. For above-bandgap excitation, the response is dominated by a photocurrent^{18–24} with a temporally step-like onset and, thus, a generally smaller bandwidth than optical rectification⁹. Apart from rare exceptions¹⁴, however, most semiconductors used are polar^{1,2,12,13,15–17,21,22} and strongly attenuate terahertz radiation around the optical phonon resonances, thereby preventing emission in the so-called reststrahlen band located between ~1 and 15 THz.

The most promising sources covering the full terahertz window so far are photocurrents in transient gas plasmas^{9,10,25–29}. The downside of this appealing approach is that the underlying ionization process usually requires amplified laser pulses with high threshold energies on the order of 0.1 mJ. Measurable terahertz waveforms

can be obtained with pump-pulse energies down to ~1 μJ (ref. 29), which are, however still two to three orders of magnitude larger than those provided by low-cost femtosecond laser oscillators.

Metals are another promising material class for realizing terahertz sources³⁰, because they exhibit a pump absorptivity largely independent of wavelength³¹, short electron lifetimes of ~10 to 50 fs (ref. 32; implying broadband photocurrents), a featureless terahertz refractive index³³ (favouring gap-free emission) and large heat conductivity (for efficient removal of excess heat). In addition, metal thin-film stacks (heterostructures) are well established, simple and cheap to fabricate. Recent works have indeed demonstrated terahertz emitters based on metal structures^{34–37}. However, the bandwidth did not exceed 3 THz, and terahertz field amplitudes competitive with those of ZnTe emitters were obtained only in conjunction with amplified laser pulses^{36,37}. Consequently, the full potential of metal-based terahertz emitters is far from being realized.

At this point, it is important to acknowledge that all previously demonstrated terahertz emitters have taken advantage exclusively of the charge but not the spin of the electron. On the other hand, very recent tremendous progress in the fields of spintronics^{38–41} and femtomagnetism^{42,43} has shown that the electron spin offers entirely new possibilities for the generation of transient currents in metals. In fact, spin-to-charge conversion has been revealed lately as a new pathway to ultrafast photocurrents^{44,45}.

In this Article, we exploit the unique spintronic and photonic properties of ultrathin metal films to realize a terahertz emitter driven by ~1 nJ laser pulses from a compact, high-repetition-rate femtosecond laser oscillator. The new source combines various benefits in one device: large bandwidth, large terahertz field

¹Department of Physical Chemistry, Fritz Haber Institute of the Max Planck Society, 14195 Berlin, Germany. ²Institute of Physics, Johannes Gutenberg University, 55128 Mainz, Germany. ³Singulus Technologies AG, 63796 Kahl am Main, Germany. ⁴Institute of Physics, Ernst Moritz Arndt University, 17489 Greifswald, Germany. ⁵Department of Physics, University of Maryland Baltimore County, Baltimore, Maryland 21250, USA. ⁶Department of Physics and Astronomy, Uppsala University, SE-75120 Uppsala, Sweden. ⁷Peter Grünberg Institute and Institute for Advanced Simulation, Forschungszentrum Jülich and JARA, 52425 Jülich, Germany. ⁸Institute for Optics and Atomic Physics, Technical University Berlin and Helmholtz-Zentrum Berlin für Materialien und Energie, 12489 Berlin, Germany. ⁹Institut de Physique et Chimie des Matériaux de Strasbourg, 67200 Strasbourg, France. ¹⁰Max Planck Institute for Polymer Research, 55128 Mainz, Germany. *e-mail: kampfrath@fhi-berlin.mpg.de

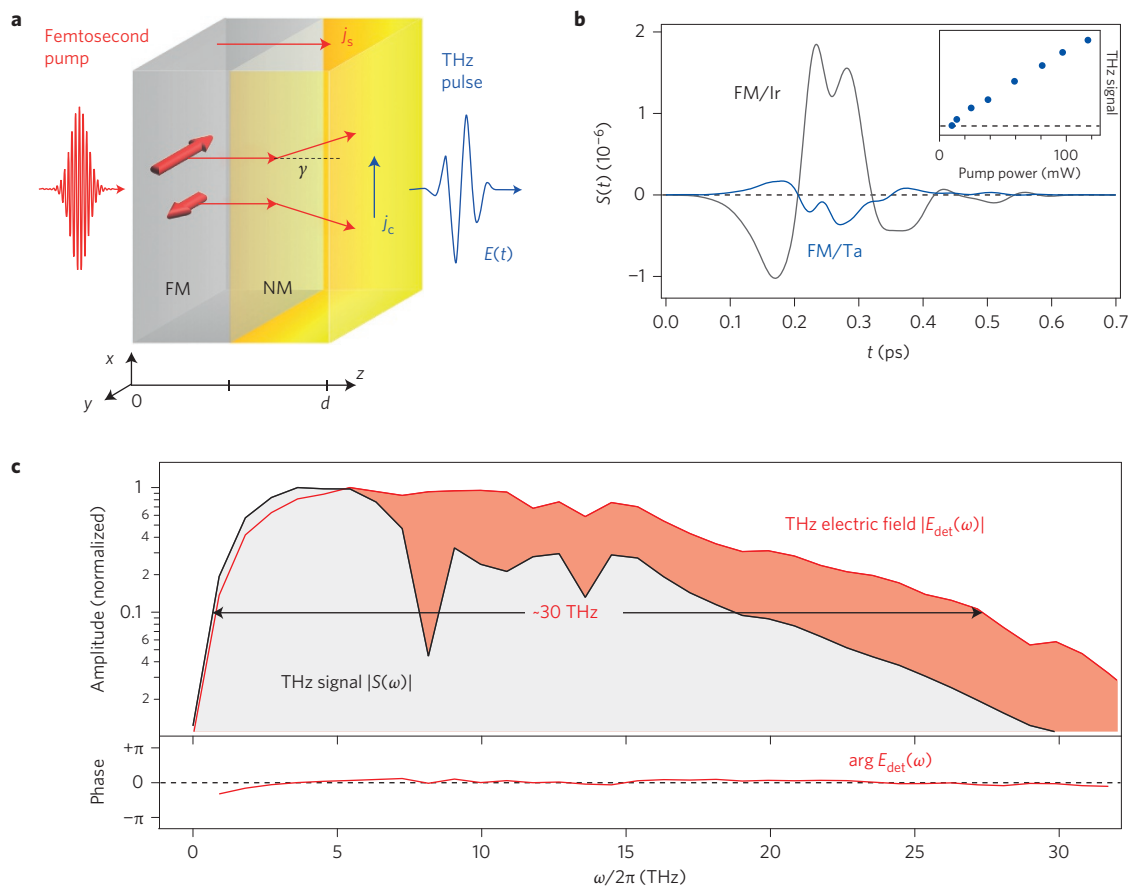


Figure 1 | Metallic spintronic terahertz emitter. **a**, Principle of operation. A femtosecond laser pulse excites electrons in the metal stack, thereby changing their band velocity and launching a current along the z direction. Because in the FM layer the mobility of spin-up (majority) electrons is significantly higher than that of spin-down (minority) electrons, the z current is spin-polarized. In the NM layer, spin-orbit interaction deflects spin-up and spin-down electrons in opposite directions and transforms the spin current j_s into an ultrafast transverse charge current $j_c = \gamma j_s$, leading to the emission of a terahertz electromagnetic transient. **b**, Typical electrooptic signal $S(t)$ of terahertz pulses obtained from photoexcited Ta- and Ir-capped $\text{Co}_{20}\text{Fe}_{60}\text{B}_{20}$ thin films and detected by a 50- μm -thick GaP crystal. Inset: Terahertz signal amplitude as a function of incident pump power. **c**, Fourier spectra of terahertz signal $S(t)$ and the extracted transient terahertz electric field $E_{\text{det}}(t)$ incident on the electrooptic detector. Both spectra are normalized to peak amplitude 1. The double-headed arrow illustrates the ~ 30 THz large bandwidth of the emitter. The flat spectral phase indicates that the terahertz pulse is Fourier-limited.

amplitude at low pump power, easy operation, scalability and low cost. This achievement becomes possible because our widely tunable approach provides access to a large set of spintronic metals and geometrical parameters for optimization.

Spintronic terahertz emitter

Figure 1a illustrates the basic principle of our spintronic terahertz emitter, with a bilayer structure consisting of ferromagnetic (FM) and nonferromagnetic (NM) metal thin films⁴⁴. The FM layer is magnetized in-plane, antiparallel to the y axis. An incident femtosecond laser pulse excites electrons in the metals to states above the Fermi energy, thereby changing their band velocity and scattering rate. Because the FM and NM layers have different transport properties, a net current along the z axis is launched. In addition, because the product of the density, band velocity and lifetime of spin-up (majority) electrons in FM metals (such as Fe, Co and Ni) is significantly higher than that of the spin-down (minority) electrons^{32,46}, the z current is strongly spin-polarized⁴².

On entering the NM layer, spin-orbit coupling deflects spin-up and spin-down electrons in opposite directions^{38–41} by a mean angle γ (Fig. 1a). This inverse spin-Hall effect (ISHE) converts the longitudinal (z -directed) spin current density j_s into an ultrafast transverse (x -directed) charge current density $j_c = \gamma j_s$, thereby acting as a source of terahertz radiation (Fig. 1a).

In our experiment, the metal stack was excited by femtosecond pulses from a Ti:sapphire laser oscillator (duration 10 fs, centre wavelength 800 nm, pulse energy 2.5 nJ, repetition rate 80 MHz). The transient electric field of the emitted terahertz pulse was measured by electrooptic sampling^{1,2,47} in suitable materials (see Methods). We started with bilayers consisting of **FM $\text{Co}_{20}\text{Fe}_{60}\text{B}_{20}$ (thickness of 3 nm) capped by either NM Ta or Ir (3 nm)** (see Methods). Typical terahertz electrooptic signals $S(t)$ obtained from these samples magnetized along the y axis (Fig. 1a) are presented in Fig. 1b. Consistent with the generation mechanism outlined above⁴⁴, the emitted radiation has the following properties (Supplementary Fig. 4). **It is linearly polarized, with the electric-field direction perpendicular to the sample magnetization, but it is independent of the pump polarization.** The spin current and thus the terahertz field are reversed entirely, either when the external saturating magnetic field of 10 mT is reversed or when the two metallic films are grown in reverse order on the substrate. Finally, the terahertz signal amplitude grows linearly with the pump power (Fig. 1b, inset). Therefore, signal saturation due to pump-induced sample demagnetization is negligible here, consistent with the estimate that ultrafast magnetization quenching is less than 1% at the maximum pump fluence used⁴⁴.

Fourier-transforming the time-domain signals $S(t)$ yields the spectral amplitude $|S(\omega)|$ versus frequency $\omega/2\pi$. A typical spectrum

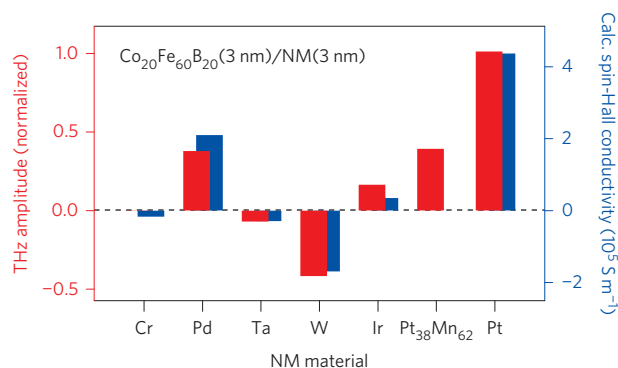


Figure 2 | Impact of the NM material. Terahertz signal amplitude (r.m.s.) as a function of the NM material used for the $\text{Co}_{20}\text{Fe}_{60}\text{B}_{20}(3\text{ nm})/\text{NM}(3\text{ nm})$ stack (red bars). For comparison, *ab initio* calculated values of the spin-Hall conductivity are also shown (blue bars), except for $\text{Pt}_{38}\text{Mn}_{62}$. A Cr cap layer leads to a nearly vanishing terahertz signal.

is shown in Fig. 1c. It covers a large bandwidth from ~ 1 to 18 THz. Note that spectral features such as the dip at 8 THz arise from the 50- μm -thick GaP electrooptic sensor and not from the emitter^{44,47}. By deconvoluting the detector response function from the signal $S(t)$, we obtain the terahertz electric field $E_{\text{det}}(t)$ directly in front of the detection crystal (see Methods). Strikingly, the field spectrum $|E_{\text{det}}(\omega)|$ (Fig. 1c) is remarkably smooth and extends from 1 to nearly 30 THz full-width at 10% amplitude maximum, without any gaps. In addition, the spectral phase of the transient field is flat (Fig. 1c), demonstrating that the terahertz pulse is Fourier-limited.

Although its bandwidth is already remarkably large, the $\text{Co}_{20}\text{Fe}_{60}\text{B}_{20}/\text{Ta}$ bilayer (Fig. 1b) generates a terahertz peak signal that is about two orders of magnitude smaller than that obtained from a standard emitter in linear terahertz spectroscopy⁹, a 1-mm-thick ZnTe(110) crystal (Fig. 4a). To boost the emitted terahertz field, we need to understand the key factors that determine it. The amplitude of the x -polarized terahertz field (Fig. 1a) directly behind the multilayer is given by (see Methods)

$$E(\omega) = Z(\omega)e \int_0^d dz \gamma(z)j_s(z, \omega) \quad (1)$$

where d is the film thickness, and e is the elementary charge. According to this generalized Ohm's law, the emitted field $E(\omega)$ equals the total charge current $-efdz \gamma j_s$ times an impedance $-Z(\omega)$, which quantifies how efficiently a current is converted into

electromagnetic radiation. Here, $1/Z$ can be interpreted as the effective conductance of a parallel connection of all metal layers shunted by the adjacent substrate and air half-spaces (see Methods).

Equation (1) readily shows that maximizing Z , γ and j_s will lead to maximum terahertz output of the emitter for a given pump power. The numerous sample parameters that can be tuned in such an optimization are the FM/NM materials and the geometry of the heterostructure.

Maximizing the terahertz output

We started by varying the NM material, which primarily affects the emitted terahertz field through the magnitude and sign of the spin-Hall angle γ (equation (1)). In particular, we considered such metals for which large γ values have been reported³⁹. Importantly, for all samples studied here, we found emitted terahertz waveforms and spectra with shapes that are very similar to those shown in Fig. 1b,c. It is therefore sufficient to quantify the strength of the emitted terahertz field by the root mean square (r.m.s.) of the terahertz signal $S(t)$. This quantity is displayed in Fig. 2 as a function of the NM metal in $\text{Co}_{20}\text{Fe}_{60}\text{B}_{20}(3\text{ nm})/\text{NM}(3\text{ nm})$ heterostructures.

Figure 2 clearly shows that the terahertz field amplitude and polarity depend drastically on the NM material chosen. For instance, Pt delivers a one order of magnitude larger amplitude than Ta and Ir. Interestingly, choosing W for the NM layer leads to a comparable magnitude as with Pd or Pt, but with opposite sign. The sign change is consistent with the findings in previous works³⁹ and is related to there being a half-filled electronic d shell in W but an almost full d shell in Pt (ref. 48). More generally, we find that the entire trend of terahertz amplitude versus NM material (Fig. 2) is in good semiquantitative agreement with the spin-Hall conductivities measured previously³⁹ and calculated by us (Fig. 2; see Methods). This observation provides further evidence for the transport scenario outlined in Fig. 1a and ref. 44.

In contrast to the NM material, the terahertz signal amplitude is found to change only relatively little when the FM material $\text{Co}_{20}\text{Fe}_{60}\text{B}_{20}$ is substituted by Fe, Co, Fe-Co alloys or $\text{Ni}_{81}\text{Fe}_{19}$ (Supplementary Section 1). In essence, varying the materials forming the FM/NM bilayers shows that the combination $\text{Co}_{40}\text{Fe}_{40}\text{B}_{20}/\text{Pt}$ provides the best terahertz-emission performance.

In the next optimization step, we varied the stack geometry and measured the terahertz emission as a function of total sample thickness d while keeping the FM and NM layers approximately equally thick. The experiment revealed a surprising dependence (Fig. 3a): the terahertz amplitude increases with decreasing emitter thickness d , peaks at $d = 4\text{ nm}$, and falls off rapidly at smaller d .

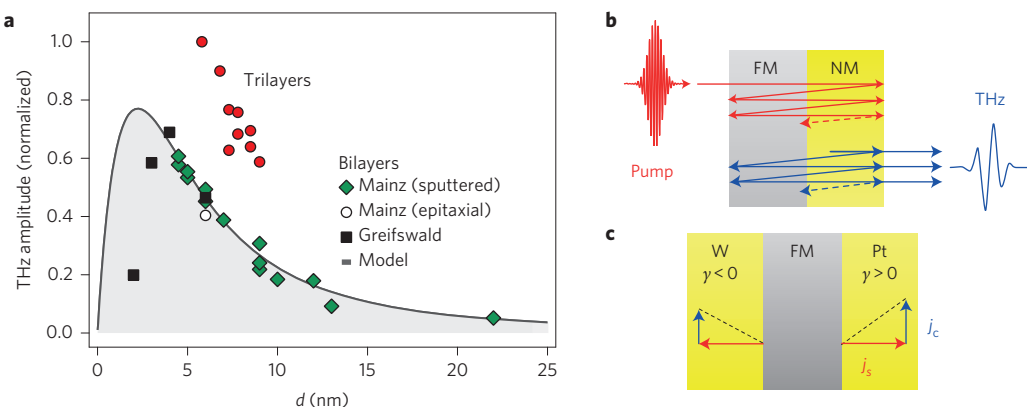


Figure 3 | Impact of stack geometry on emitter performance. **a**, Terahertz signal amplitude (r.m.s.) as a function of thickness d of the metal stack. Different symbols represent different sample fabrication schemes (see Methods). The solid line is a fit using a transport model (main text and Methods). **b**, Schematic of the thin-film Fabry-Pérot cavity that enhances both the incident pump and emitted terahertz radiation. **c**, Schematic of the trilayer emitter that converts the backward- and forward-flowing spin current j_s into a unidirectional charge current j_c with approximately equal efficiency.

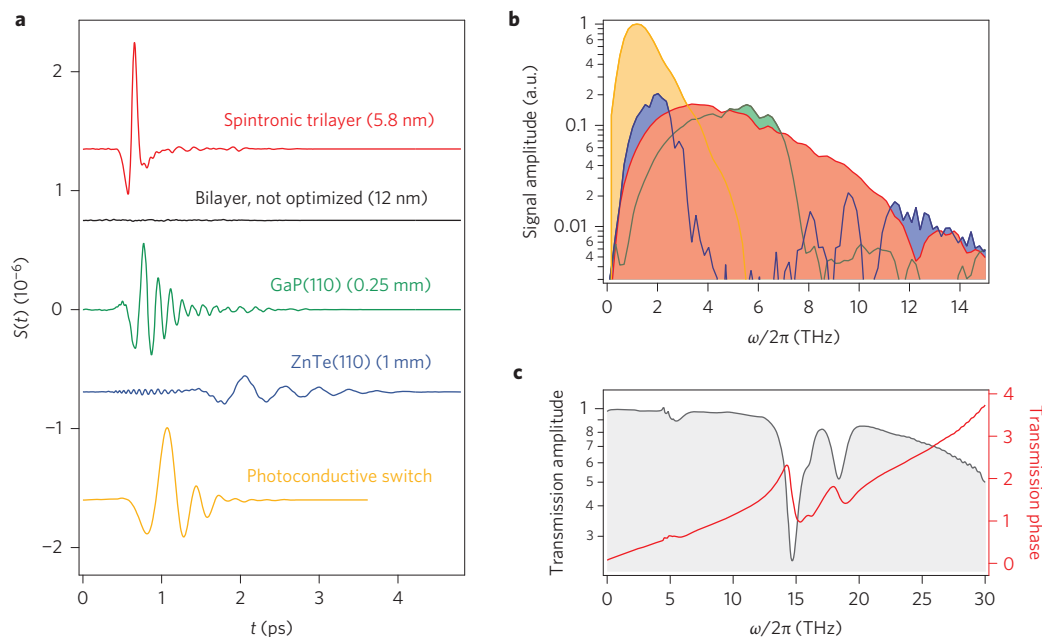


Figure 4 | Spintronic emitter performance and spectroscopic application. **a, b**, Terahertz signal waveforms (**a**) and resulting amplitude spectra (**b**) of the spintronic trilayer emitter in comparison to standard terahertz emitters as measured with a 70- μm -thick LAPC electrooptic sensor. Measurements were performed under identical conditions so that the output of all emitters can be compared directly. Deconvolution of the detector response function yields the transient terahertz electric fields, which are shown in Supplementary Fig. 1. **c**, Spectral amplitude and phase of the terahertz transmission of a 7.5- μm -thick PTFE thread-seal tape measured with our spintronic emitter using a 10- μm -thick ZnTe electrooptic sensor.

This behaviour is highly counterintuitive and in sharp contrast to most phase-matched frequency conversion schemes such as optical rectification and second-harmonic generation⁹. Indeed, equation (1) suggests that the terahertz field amplitude scales with metal thickness d . This trend, however, is overcompensated by a remarkable photonic effect: our metal thin film acts as a Fabry–Pérot cavity that resonantly enhances both pump and terahertz waves. As the cavity length d is much smaller than all wavelengths involved, all reflection echoes inside the film interfere constructively (Fig. 3b). The shorter the cavity, the more echoes occur before the light wave has decayed, resulting in even more enhancement. Below a critical thickness d_c , however, reflection losses at the cavity faces exceed attenuation in the metal bulk. The enhancement of the pump and terahertz electric field then saturates at $d < d_c$ and no longer compensates for the shrinking emitter volume. The emitted terahertz amplitude should first grow with decreasing d and, after reaching a maximum, decrease, in agreement with our experimental data (Fig. 3a).

A quantitative description of this behaviour is provided by equation (1) and a simple transport model for j_s (see Methods). The best fit (solid curve in Fig. 3a) is obtained when we assume that the spin-polarized carriers entering the Pt layer randomize their velocity over a length of 1 nm. In essence, Fig. 3a shows that the largest terahertz signal is provided by the 4-nm-thick $\text{Co}_{20}\text{Fe}_{60}\text{B}_{20}/\text{Pt}$ emitter, and this performance is very close to the absolute maximum predicted by our model.

Having identified the best bilayer emitter, we finally tailored the sequence of the spintronic metal layers. Figure 1a suggests that only the forward-propagating half of the photoinduced spin current travels into the NM layer where it is converted into a charge current. To also take advantage of the backward-flowing electrons, we introduced another NM layer on the left-hand side of the FM film (Fig. 3c). We chose $\text{W}/\text{Co}_{40}\text{Fe}_{40}\text{B}_{20}/\text{Pt}$, because W and Pt exhibit the largest spin-Hall angles γ , but with opposite sign (Fig. 2). Because of this unique possibility for spintronic engineering, the spin-Hall currents j_c in the W and Pt layer flow in the

same direction, radiate in phase and thus, again, boost the terahertz amplitude (Fig. 3c).

Indeed, as seen in Fig. 3a, the terahertz amplitude from each $\text{W}/\text{Co}_{40}\text{Fe}_{40}\text{B}_{20}/\text{Pt}$ trilayer is approximately twice as high as that from a bilayer counterpart with the same total thickness. In particular, the $\text{W}(2\text{ nm})/\text{Co}_{40}\text{Fe}_{40}\text{B}_{20}(1.8\text{ nm})/\text{Pt}(2\text{ nm})$ trilayer delivers a 40% higher terahertz amplitude than the best bilayer $\text{Co}_{20}\text{Fe}_{60}\text{B}_{20}(2\text{ nm})/\text{Pt}(2\text{ nm})$, even though the trilayer is $\sim 50\%$ thicker. This result indicates that the conversion of both forward and backward spin currents into terahertz radiation overcompensates the effect of the larger metal thickness.

Figure 3a concludes our model-guided optimization strategy and identifies the 5.8-nm-thick $\text{W}/\text{Co}_{40}\text{Fe}_{40}\text{B}_{20}/\text{Pt}$ trilayer as the best terahertz emitter out of the comprehensive set of more than 70 heterostructures studied here. With this extensive procedure, we have gone beyond all previous approaches for emitter design and have fully exploited the spintronic nature of our terahertz source. The evolution of our efforts is illustrated in Fig. 4a. The trilayer delivers a more than two orders of magnitude larger terahertz amplitude than $\text{Co}_{20}\text{Fe}_{60}\text{B}_{20}(10\text{ nm})/\text{Ta}(2\text{ nm})$, which is one of the bilayers we first investigated.

Performance test

To evaluate the performance of our trilayer emitter, we compared it to three state-of-the-art terahertz sources routinely used to cover the range from ~ 0.3 to 8 THz: the nonlinear optical crystals ZnTe(110) and GaP(110)^{1,9} and a high-performance photoconductive switch biased by interdigitated electrodes²² (see Methods). For all the emitters, terahertz emission was measured under identical conditions, and the terahertz signal amplitude was found to scale linearly with pump power. Consequently, a comparison of the terahertz spectral amplitudes provides a direct measure of how well each emitter performs at a given frequency. To directly identify spectral emission gaps, we chose a 70- μm -thick Lemke/amorphous polycarbonate (LAPC) electrooptic sensor¹⁴ that permits gap-free detection from ~ 0.3 to 15 THz (Supplementary Fig. 2).

Figure 4a,b displays terahertz waveforms $S(t)$ from all sources and the respective amplitude spectra. The resulting transient terahertz electric fields (see Methods) are shown in Supplementary Fig. 1. For ZnTe and GaP, the electrooptic signal $S(t)$ consists of slowly and quickly oscillating sections, which are, respectively, related to frequencies below and above the reststrahlen band of these crystals. Strong wave attenuation in the reststrahlen region⁴⁷ leads to considerable gaps from 3 to 10 THz and 7 to 13 THz in the ZnTe and GaP amplitude spectra $|S(\omega)|$, respectively (Fig. 4b). In contrast, the time-domain signal from the spintronic trilayer features a higher peak amplitude, is much shorter (Fig. 4a) and even Fourier-limited (Fig. 1c). Remarkably, the spectrum is gap-free and exceeds the spectral amplitude of the ZnTe and GaP crystals from 2.5 to 14 THz, except small frequency intervals around 6 and 12 THz where GaP and ZnTe, respectively, yield slightly more amplitude. We note that our trilayer emitter is characterized by an effective $\chi^{(2)}$ nonlinear optical coefficient that is five orders of magnitude larger than that of GaP (Supplementary Section 2). As revealed above, this coefficient is, however, confined to an only ~ 1 -nm-thick layer at the FM/NM interfaces.

Although the photoconductive switch and the trilayer exhibit comparable terahertz signal amplitudes in the time domain (Fig. 4a), their performance is complementary in frequency space (Fig. 4b). In the case where exceptionally high amplitudes are required below 3 THz, the photoconductive switch is the source of choice. In contrast, the spintronic emitter provides more amplitude above 3 THz and exhibits a much wider bandwidth from 1 to 30 THz without a gap (Supplementary Fig. 1).

We routinely use our trilayer emitter to measure ultrabroadband terahertz transmission spectra. As an example, Fig. 4c displays the amplitude and phase of the complex-valued transmission of a 7.5- μm -thick polytetrafluoroethylene (PTFE, Teflon) sample, obtained using the trilayer emitter and a 10- μm -thick ZnTe(110) electrooptic sensor⁴⁷. Resonant features around 6, 15 and 18 THz are found, in excellent agreement with previous studies⁴⁹ using gas-plasma terahertz emitters that were, however, driven by five orders of magnitude more intense pump pulses. We finally note that such broadband and gapless terahertz spectroscopy would not be possible at all with standard solid-state emitters.

Conclusion

We have developed a conceptually new, high-performance and versatile terahertz source for broadband linear terahertz spectroscopy based on optically driven spin currents in ultrathin magnetic metal heterostructures. Our approach unifies the benefits of different emitter types in one device: it approaches the bandwidth of the much more expensive gas-plasma spectroscopy systems and delivers short, Fourier-limited pulses covering the full range from 1 to 30 THz without a gap. As with often-used optical-rectification crystals, our heterostructure is robust, passive, easy to use (in transmission mode under normal incidence) and driven by a low-cost, compact femtosecond laser oscillator. At the same time, the terahertz field amplitude emitted exceeds that of standard emitters such as ZnTe, GaP and a biased photoconductive switch. Similar to such switches, the direction and amplitude of the emitted terahertz field can be modulated easily by applying an oscillating magnetic field with small amplitude below 10 mT. In addition to these benefits, the broadband optical absorption of metals implies that the spintronic terahertz source can be driven by any laser oscillator, virtually independent of its output wavelength.

We emphasize that the fabrication of our emitter is inexpensive, straightforward and scalable, without involving any lithography steps. Fabrication costs are dominated by the substrate price, and we are able to deposit homogeneous layers on substrates with diameters as large as 20 cm (see Methods). Preliminary tests show that driving such large-area trilayers with intense laser pulses easily

yields terahertz pulses with peak fields of several 100 kV cm⁻¹, which exceed those obtained with more strongly pumped large-area ZnTe emitters⁵⁰. Therefore, spintronic terahertz sources exhibit a high potential for enabling nonlinear optical studies^{51,52} in the difficult to access region between 5 and 10 THz. More generally, our results highlight metallic magnetic multilayers as a new and very promising class of high-performance and broadband terahertz emitters. Finally, this work is an example of a rapid translation of recently discovered fundamental physical effects into useful technology that can straightforwardly be employed by the broad femtosecond-laser community.

Methods

Methods and any associated references are available in the [online version of the paper](#).

Received 18 September 2015; accepted 8 April 2016;
published online 23 May 2016

References

- Ferguson, B. & Zhang, X. Materials for terahertz science and technology. *Nature Mater.* **1**, 26–33 (2002).
- Tonouchi, M. Cutting-edge terahertz technology. *Nature Photon.* **1**, 97–105 (2007).
- Ulbricht, R., Hendry, E., Shan, J., Heinz, T. & Bonn, M. Carrier dynamics in semiconductors studied with time-resolved terahertz spectroscopy. *Rev. Mod. Phys.* **83**, 543–586 (2011).
- Kampfthar, T., Tanaka, K. & Nelson, K. Resonant and nonresonant control over matter and light by intense terahertz transients. *Nature Photon.* **7**, 680–690 (2013).
- Chan, W., Deibel, J. & Mittleman, D. Imaging with terahertz radiation. *Rep. Prog. Phys.* **70**, 1325–1379 (2007).
- Cocker, T. L. *et al.* An ultrafast terahertz scanning tunnelling microscope. *Nature Photon.* **7**, 620–625 (2013).
- Sano, Y. *et al.* Imaging molecular adsorption and desorption dynamics on graphene using terahertz emission spectroscopy. *Sci. Rep.* **4**, 6046 (2014).
- Zeitler, J. *et al.* Terahertz pulsed spectroscopy and imaging in the pharmaceutical setting—a review. *J. Pharm. Pharmacol.* **59**, 209–223 (2007).
- Reimann, K. Table-top sources of ultrashort THz pulses. *Rep. Prog. Phys.* **70**, 1597–1632 (2007).
- Blanchard, F. *et al.* Generation of intense terahertz radiation via optical methods. *IEEE J. Sel. Top. Quantum Electron.* **17**, 5–16 (2011).
- Rice, A. *et al.* Terahertz optical rectification from (110) zinc-blende crystals. *Appl. Phys. Lett.* **64**, 1324–1326 (1994).
- Kaindl, R., Eickemeyer, F., Woerner, M. & Elsaesser, T. Broadband phase-matched difference frequency mixing of femtosecond pulses in GaSe: experiment and theory. *Appl. Phys. Lett.* **75**, 1060–1062 (1999).
- Huber, R., Brodschelm, A., Tauser, F. & Leitenstorfer, A. Generation and field-resolved detection of femtosecond electromagnetic pulses tunable up to 41 THz. *Appl. Phys. Lett.* **76**, 3191–3193 (2000).
- Zheng, X., Sinyukov, A. & Hayden, L. M. Broadband and gap-free response of a terahertz system based on a poled polymer emitter–sensor pair. *Appl. Phys. Lett.* **87**, 081115 (2005).
- Zheng, X., McLaughlin, C. V., Cunningham, P. & Hayden, L. M. Organic broadband terahertz sources and sensors. *J. Nanoelectron. Optoelectron.* **2**, 58–76 (2007).
- Brunner, F. *et al.* A hydrogen-bonded organic nonlinear optical crystal for high-efficiency terahertz generation and detection. *Opt. Express* **16**, 16496–16508 (2008).
- Katayama, I. *et al.* Ultrabroadband terahertz generation using 4-*N,N*-dimethylamino-4'-*N'*-methyl-stilbazolium tosylate single crystals. *Appl. Phys. Lett.* **97**, 021105 (2010).
- Shan, J. & Heinz, T. F. in *Ultrafast Dynamical Processes in Semiconductors* (ed. Tsen, K.-T.) 1–56 (Springer, 2004).
- Apostolopoulos, V. & Barnes, M. THz emitters based on the photo-Dember effect. *J. Phys. D* **47**, 374002 (2014).
- Klatt, G. *et al.* Terahertz emission from lateral photo-Dember currents. *Opt. Express* **18**, 4939–4947 (2010).
- Shen, Y., Upadhyay, P., Linfield, E., Beere, H. & Davies, A. Ultrabroadband terahertz radiation from low-temperature-grown GaAs photoconductive emitters. *Appl. Phys. Lett.* **83**, 3117–3119 (2003).
- Winnerl, S. Scalable microstructured photoconductive terahertz emitters. *J. Infrared Millim. Terahertz Waves* **33**, 431–454 (2012).
- Hale, P. *et al.* 20 THz broadband generation using semi-insulating GaAs interdigitated photoconductive antennas. *Opt. Express* **22**, 26358–26364 (2014).

24. Berry, C., Wang, N., Hashemi, M., Unlu, M. & Jarrahi, M. Significant performance enhancement in photoconductive terahertz optoelectronics by incorporating plasmonic contact electrodes. *Nature Commun.* **4**, 1622 (2013).
25. Thomson, M. D., Krefß, M., Löffler, T. & Roskos, H. G. Broadband THz emission from gas plasmas induced by femtosecond optical pulses: from fundamentals to applications. *Laser Photon. Rev.* **1**, 349–368 (2007).
26. Kim, K., Glowina, J., Taylor, A. J. & Rodriguez, G. High-power broadband terahertz generation via two-color photoionization in gases. *IEEE J. Quantum Electron.* **48**, 797–805 (2012).
27. Lu, X. & Zhang, X. C. Investigation of ultra-broadband terahertz time-domain spectroscopy with terahertz wave gas photonics. *Front. Optoelectron.* **7**, 121–155 (2013).
28. Bartel, T., Gaal, P., Reimann, K., Woerner, M. & Elsaesser, T. Generation of single-cycle THz transients with high electric-field amplitudes. *Opt. Lett.* **30**, 2805–2807 (2005).
29. Buccheri, F. & Zhang, X. C. Terahertz emission from laser-induced microplasma in ambient air. *Optica* **2**, 366–369 (2015).
30. Ramanandan, G., Ramakrishnan, G., Kumar, N., Adam, A. & Planken, P. Emission of terahertz pulses from nanostructured metal surfaces. *J. Phys. D* **47**, 374003 (2014).
31. Zhang, L. *et al.* High-power THz to IR emission by femtosecond laser irradiation of random 2D metallic nanostructures. *Sci. Rep.* **5**, 12536 (2015).
32. Zhukov, V., Chulkov, E. & Echenique, P. Lifetimes and inelastic mean free path of low-energy excited electrons in Fe, Ni, Pt, and Au: *ab initio* GW + T calculations. *Phys. Rev. B* **73**, 125105 (2006).
33. Laman, N. & Grischkowsky, D. Terahertz conductivity of thin metal films. *Appl. Phys. Lett.* **93**, 051105 (2008).
34. Ramakrishnan, G. & Planken, P. Percolation-enhanced generation of terahertz pulses by optical rectification on ultrathin gold films. *Opt. Lett.* **36**, 2572–2574 (2011).
35. Polyushkin, D., Hendry, E., Stone, E. & Barnes, W. THz generation from plasmonic nanoparticle arrays. *Nano Lett.* **11**, 4718–4724 (2011).
36. Kadlec, F., Kuzel, P. & Coutaz, J. Study of terahertz radiation generated by optical rectification on thin gold films. *Opt. Lett.* **30**, 1402–1404 (2005).
37. Welsh, G. H., Hunt, N. T. & Wynne, K. Terahertz-pulse emission through laser excitation of surface plasmons in a metal grating. *Phys. Rev. Lett.* **98**, 026803 (2007).
38. Saitoh, E., Ueda, M., Miyajima, H. & Tataru, G. Conversion of spin current into charge current at room temperature: inverse spin-Hall effect. *Appl. Phys. Lett.* **88**, 182509 (2006).
39. Hoffmann, A. Spin Hall effects in metals. *IEEE Trans. Magn.* **49**, 5172–5193 (2013).
40. Sinova, J. *et al.* Spin Hall effects. *Rev. Mod. Phys.* **87**, 1213–1260 (2015).
41. Wei, D. *et al.* Spin Hall voltages from a.c. and d.c. spin currents. *Nature Commun.* **5**, 3768 (2014).
42. Battiato, M., Carva, K. & Oppeneer, P. M. Superdiffusive spin transport as a mechanism of ultrafast demagnetization. *Phys. Rev. Lett.* **105**, 027203 (2010).
43. Melnikov, A. *et al.* Ultrafast transport of laser-excited spin polarized carriers in Au/Fe/MgO(001). *Phys. Rev. Lett.* **107**, 076601 (2011).
44. Kampfrath, T. *et al.* Terahertz spin current pulses controlled by magnetic heterostructures. *Nature Nanotech.* **8**, 256–260 (2013).
45. Héroux, J. B., Ino, Y., Kuwata-Gonokami, M., Hashimoto, Y. & Katsumoto, S. Terahertz radiation emission from GaMnAs. *Appl. Phys. Lett.* **88**, 221110 (2006).
46. Jin, Z. *et al.* Accessing the fundamentals of magnetotransport in metals with terahertz probes. *Nature Phys.* **11**, 761–766 (2015).
47. Leitenstorfer, A., Hunsche, S., Shah, J., Nuss, M. & Knox, W. Detectors and sources for ultrabroadband electro-optic sampling: experiment and theory. *Appl. Phys. Lett.* **74**, 1516–1518 (1999).
48. Kontani, H., Tanaka, T., Hirashima, D., Yamada, K. & Inoue, J. Giant orbital Hall effect in transition metals: origin of large spin and anomalous Hall effects. *Phys. Rev. Lett.* **102**, 016601 (2009).
49. D'Angelo, F., Mics, Z., Bonn, M. & Turchinovich, D. Ultra-broadband THz time-domain spectroscopy of common polymers using THz air photonics. *Opt. Express* **22**, 12475–12485 (2014).
50. Blanchard, F. *et al.* Generation of 1.5 μ J single-cycle terahertz pulses by optical rectification from a large aperture ZnTe crystal. *Opt. Express* **15**, 13212–13220 (2007).
51. Liu, M. *et al.* Terahertz-field-induced insulator-to-metal transition in vanadium dioxide metamaterial. *Nature* **487**, 345–348 (2012).
52. Vicario, C. *et al.* Off-resonant magnetization dynamics phase-locked to an intense phase-stable terahertz transient. *Nature Photon.* **7**, 720–723 (2013).

Acknowledgements

The authors thank S. Winnerl for providing a TeraSED3 emitter and for stimulating discussions. The authors acknowledge the German Science Foundation for funding through SPP 1538/SpinCaT (Berlin, Greifswald, Jülich and Mainz groups) and through SFB TRR 173/Spin+X (Mainz group). The European Union is acknowledged for funding through ERC H2020 CoG project TERAMAG/grant no. 681917 (T.K.), FP7 project CRONOS/grant no. 280879 (T.K. and M.W.), FP7 Marie Curie ITN WALL project/grant no. 608031 (J.S., G.J. and M.K.), Career Integration Grant LIGHTER/grant no. 334324 (D.T.) and FP7 project FemtoSpin/grant no. 281043 (P.M. and P.M.O.). The authors are grateful for support from the Max Planck Society (T.K. and D.T.), the Swedish Research Council, the Röntgen-Ångström Cluster, and the K. and A. Wallenberg Foundation (P.M. and P.M.O.), the Samsung SGMI programme, the EFRE Program of the state of Rhineland Palatinate, TT-DINEMA, the Excellence Graduate School MAINZ (GSC 266) and the state research centre CINEMA (Mainz group). F.F. and Y.M. acknowledge Jülich Supercomputing Centre for computing time.

Author contributions

T.K. and T.S. conceived the experiments. T.K. and I.R. carried out preliminary measurements. S.J., U.M., A.K., J.He., E.B., M.J., G.J., M.M. and M.K. fabricated the spintronic emitters and optimized the fabrication process. L.B., T.S. and T.K. built the terahertz emission set-up. J.Ha. and L.M.H. fabricated the LAPC electrooptic detectors. T.S. performed the terahertz experiments and optical sample characterization. T.S. and T.K. analysed experimental data with contributions from D.T. and M.K. T.K. and T.S. developed the analytical terahertz-emitter model with contributions from F.F. and Y.M. F.F. and Y.M. calculated spin-Hall conductivities. P.M. and P.M.O. conducted calculations of the ultrafast spin transport. T.K., T.S., D.T., M.W. and M.K. co-wrote the paper. All authors contributed to discussing the results and writing the paper.

Additional information

Supplementary information is available in the [online version of the paper](#). Reprints and permissions information is available online at www.nature.com/reprints. Correspondence and requests for materials should be addressed to T.K.

Competing financial interests

The authors declare no competing financial interests.

Methods

Sample fabrication. The magnetic heterostructures were grown on glass, sapphire or MgO substrates. Most of the samples from the Mainz group were fabricated using an Ar sputter deposition tool (Singulus Rotaris) with targets of 100 nm diameter. Typically, the Ar pressure range was 2×10^{-3} mbar to 4×10^{-3} mbar, the power used was 800 W, and the deposition rates were 1.2 Å s^{-1} for the ferromagnetic (FM) layer and 2.1 Å s^{-1} for the nonferromagnetic (NM) layer. Before deposition, a short plasma etch was performed to remove organic contaminants from the substrate surface. The epitaxial Fe(100) thin film (thickness 3 nm) was prepared by radiofrequency-sputtering on a MgO(100) substrate at room temperature. After confirmation of the epitaxial growth by reflection high-energy electron diffraction, an epitaxial Pt(100) layer (3 nm) was d.c. sputtered on top.

The $\text{Co}_{20}\text{Fe}_{60}\text{B}_{20}$ films from the Greifswald group were prepared by magnetron sputtering, and the NM metal films were grown by electron-beam evaporation under ultrahigh-vacuum conditions (base pressure of 5×10^{-10} mbar) using *in situ* transfer. Composition analysis of the films yielded a Co/Fe ratio of 1/2.1, and characterization by transmission electron microscopy revealed smooth $\text{Co}_{20}\text{Fe}_{60}\text{B}_{20}$ film surfaces below the atomic monolayer limit.

The samples exhibited typical thin-film properties⁵³, in-plane magnetic anisotropy and a nearly rectangular hysteresis curve with a coercive field well below 10 mT.

Sample optical properties. To further characterize the heterostructures, optical reflectance and transmittance were measured using the pump beam of the terahertz emission set-up (see next subsection for details). Our data (Supplementary Fig. 3) show that the multilayers absorb about 50% of the incident laser power, largely independent of the total metal thickness. The measured values of reflectance and transmittance agree excellently with calculations based on a transfer-matrix formalism⁵⁴ and literature data for the optical constants of the materials involved^{55,56}. Such good agreement is indicative of an optically homogeneous and flat metal film, as expected from the optimized film deposition.

The terahertz conductivity of the Pt and FM films was measured by terahertz transmission spectroscopy⁵⁷. We obtained values of $\sigma = (6.5 \pm 0.1) \times 10^5 \text{ S m}^{-1}$ for $\text{Co}_{40}\text{Fe}_{40}\text{B}_{20}$ and $(2.9 \pm 0.1) \times 10^6 \text{ S m}^{-1}$ for Pt, approximately independent of the terahertz frequency due to the high Drude scattering rate, which is on the order of 50 THz.

Terahertz emission set-up. In the optical experiment (Fig. 1a), the sample was kept in an external saturating magnetic field of 10 mT, and was excited by linearly polarized laser pulses (duration 10 fs, centre wavelength 800 nm, energy 2.5 nJ) from a Ti:sapphire laser oscillator (repetition rate 80 MHz) under normal incidence from the substrate side (beam diameter at sample 50 μm full-width at half-maximum of the intensity). The terahertz electric field was detected by electrooptic sampling^{1,2,47}, with probe pulses (0.6 nJ, 10 fs) from the same laser co-propagating with the terahertz field through an electrooptic crystal. The resulting signal $S(t)$ equals twice the terahertz-field-induced probe ellipticity, where t is the delay between the terahertz and probe pulse. Depending on the signal strength, duration and bandwidth required, we used various electrooptic materials: ZnTe(110) (thickness of 10 μm and 1 mm)⁴⁷, GaP(110) (50 and 250 μm)⁴⁷ and the poled-polymer guest-host system Lemke/amorphous polycarbonate (LAPC)¹⁴ (70 μm).

In the performance evaluation, the spintronic trilayer and reference emitters (Fig. 4a) were operated under identical pump-beam and detection conditions. The terahertz amplitude obtained from the commercially available photoconductive switch (TeraSED3, based on interdigitated electrodes on a semi-insulating GaAs substrate²²) was maximized by setting the d.c. bias voltage to 12 V (20% above the maximum value recommended by the technical specifications). All measurements were performed at room temperature in a N_2 atmosphere.

Signal deconvolution. To extract the terahertz electric field E_{det} incident onto the detector from the terahertz signal S measured by electrooptic sampling, we note that these waveforms are connected by the convolution

$$S(t) = (h * E_{\text{det}})(t) \quad (2)$$

The detector response function h depends on the parameters of the electrooptic crystal and the sampling pulse used^{47,58,59}. For the calculation of h , the optical constants are taken from refs 47,60 and 61. Supplementary Fig. 2 shows the spectral amplitude and phase of the calculated $h(\omega)$ for the detectors used in this work. By equidistant sampling of the measured $S(t)$ and the calculated $h(t)$, equation (2) can be rewritten as an overdetermined matrix equation and numerically solved for $E_{\text{det}}(t)$. Example traces of the absolute electric field are displayed in Supplementary Fig. 1a.

Derivation of equation (1). To derive a relationship between the emitted terahertz electric field and its source current, we note that within our sample the beam diameter is much larger than the sample thickness ($d \approx 10 \text{ nm}$). Plane-wave propagation along the z axis (Fig. 1a) is therefore assumed. The charge current density $-ej_c$ resulting from the laser-driven spin current density $(h/2)j_s$ and the inverse spin-Hall effect generates an electromagnetic wave with an electric field

$E(z, t)$ polarized along the x axis (Fig. 1a). In the frequency domain, the dynamics of E are governed by the wave equation⁶²

$$[\partial_z^2 + k^2(z, \omega)]E(z, \omega) = Q(z, \omega) = -eZ_0 \omega j_c(z, \omega)/ic \quad (3)$$

where c is the vacuum speed of light and $Z_0 = 377 \text{ }\Omega$ is the vacuum impedance. The terahertz wavevector $k(z, \omega)$ is given by $k^2 = k_0^2 + \Delta(k^2)$ where $k_0 = n\omega/c$ refers to the system without a metal film, for which the refractive index $n(z, \omega)$ equals $n_1(\omega)$ for the substrate half-space ($z < 0$) and $n_2 \approx 1$ for the air half-space ($z > 0$). When metal films are deposited on the substrate, the wavevector landscape $k_0^2(z, \omega)$ changes by $\Delta(k^2) = iZ_0\sigma\omega/c$ where $\sigma(z, \omega)$ is the conductivity distribution of the metal stack. We omit the ω dependence in the notation for brevity and rewrite equation (3) as an integral equation

$$E(z) = \int dz' [Q(z') - \Delta(k^2)(z')E(z')] G_0(z, z') \quad (4)$$

where $G_0(z, z')$ is the Green's function of the system without metal films ($k = k_0$) (ref. 62). When both source point z' and observation point z are on the air side ($z, z' > 0$), one has $G_0(z, z') = (e^{ik_0|z-z'|}/2ik_0) \cdot (1 + r_{21}e^{2ik_0|z|})$ with $k_2 = n_2\omega/c$. The term with the Fresnel coefficient $r_{21} = (n_2 - n_1)/(n_2 + n_1)$ accounts for wave reflection at the air-substrate interface at $z = 0$.

Because the film is much thinner than the wavelength and attenuation length of the terahertz wave, we approximate all phase factors by 1 and assume the electric field E is constant throughout the metal multilayer (quasistatic approximation). As a consequence, both E and $G_0 \approx (c/\omega)/(n_1 + n_2)$ can be moved in front of the integral of equation (4) and we obtain equation (1) of the main text in which the impedance is given by

$$\frac{1}{Z(\omega)} = \frac{n_1(\omega) + n_2(\omega)}{Z_0} + \int_0^d dz \sigma(z, \omega) \quad (5)$$

When the sheet conductance $\int dz \sigma$ of the metal stack is much larger than the shunt conductance $(n_1 + n_2)/Z_0$ of the two adjacent half-spaces, equation (1) turns into the familiar form of Ohm's law⁴⁴. Note that our derivation accounts for the propagation of the terahertz radiation inside the sample (including all reflection echoes) and the irradiation into free space (Fig. 3b). It is, however, restricted to the thin-film limit.

Model for metal-thickness dependence of terahertz emission. To model the terahertz emission amplitude of a FM/NM bilayer, we make use of equations (1) and (5) and assume that FM = $\text{Co}_{20}\text{Fe}_{60}\text{B}_{20}$ and NM = Pt. The impedance of the bilayer (equation (5)) is determined by the measured terahertz conductivities of the materials involved (see section 'Sample optical properties').

Equation (1) requires knowledge of the charge current density $j_c(z) = \gamma(z)j_s(z)$. To model the spatial structure of j_c , we neglect the spin-Hall angle γ in the FM layer and determine the spin current density j_s in the NM layer by considering the following simplified scenario. After excitation by the pump pulse, spin-polarized hot electrons from the FM layer enter the NM layer in which they first propagate ballistically away from the FM/NM interface (Fig. 1a). However, once an electron undergoes scattering, its velocity is randomized such that its contribution to the ultrafast photocurrent, and thus the terahertz signal, becomes negligible. To account for such velocity relaxation, we assume that the density of ballistic electrons behind the FM/NM interface decreases according to $e^{-(z-d_{\text{FM}})/\lambda_{\text{rel}}}$. Here, λ_{rel} can be considered as a hot-electron velocity relaxation length, and d_{FM} is the thickness of the FM layer. We furthermore assume that the electrons undergo perfect reflection at the NM/air and NM/FM interface.

As shown in ref. 63, these assumptions imply a spatial dependence of the ballistic spin current density inside the NM layer ($d_{\text{FM}} < z < d = d_{\text{FM}} + d_{\text{NM}}$) according to

$$j_s(z) = j_s(d_{\text{FM}}) \frac{\sinh[(z - d_{\text{FM}})/\lambda_{\text{rel}}]}{\sinh(d_{\text{NM}}/\lambda_{\text{rel}})} \quad (6)$$

where $j_s(d_{\text{FM}})$ is the spin current density directly after the FM layer. Finally, the linear fluence dependence of the emitted terahertz field (Fig. 1b) indicates that the spin current is proportional to the energy density deposited by the pump pulse. Therefore, one has $j_s(d_{\text{FM}}) \propto A/d$ where A is the absorbed fraction of the incident pump power (Supplementary Fig. 3). Inserting equation (6) and all other assumptions into equations (1) and (5), we obtain

$$E(d) \propto \gamma_{\text{NM}} \lambda_{\text{rel}} \frac{A}{d} \frac{\tanh(d_{\text{NM}}/2\lambda_{\text{rel}})}{n_1 + n_2 + Z_0 \int_0^d dz \sigma(z)} \quad (7)$$

with λ_{rel} and a global amplitude factor being the only free parameters.

The choice $\lambda_{\text{rel}} = 1 \text{ nm}$ yields the best fit to the measured thickness dependence of the emitted terahertz amplitude, including the existence of a maximum (Supplementary Fig. 6). The discrepancy for $d < 4 \text{ nm}$ (Fig. 3a) is most probably due to shortcomings of our simplified transport model and due to changes in the magnetic properties (such as the Curie temperature) of the sample when approaching small thicknesses d . For $d > 25 \text{ nm}$, we do not expect additional

Fabry–Pérot resonances for the pump beam because the decay length of the pump intensity (~ 15 nm) is much shorter than the wavelength (~ 300 nm) of the pump radiation inside the metal film.

Ab initio calculations of the spin-Hall effect. The spin-Hall conductivity (Fig. 2) was calculated using the Kubo formula within density-functional theory using the full-potential linearized augmented plane-wave (FLAPW) program FLEUR (<http://www.flapw.de>). We employed the generalized gradient approximation of the exchange correlation potential, a plane-wave cutoff at a wavevector of 85 nm^{-1} and experimental lattice constants (2.91, 3.892, 3.302, 3.166, 3.8402 and 3.926 Å for Cr, Pd, Ta, W, Ir and Pt, respectively). Further details on the computation are given in ref. 64.

References

53. Boule, O., Malinowski, G. & Kläui, M. Current-induced domain wall motion in nanoscale ferromagnetic elements. *Mater. Sci. Eng. R* **72**, 159–187 (2011).
54. Yeh, P. *Optical Waves in Layered Media* (Wiley, 2005).
55. Liang, X., Xu, X., Zheng, R., Lum, Z. & Qiu, J. Optical constant of CoFeB thin film measured with the interference enhancement method. *Appl. Opt.* **54**, 1557–1563 (2015).
56. Ordal, M., Bell, R., Alexander, R. Jr, Newquist, L. & Querry, M. Optical properties of Al, Fe, Ti, Ta, W, and Mo at submillimeter wavelengths. *Appl. Opt.* **27**, 1203–1209 (1988).
57. Nuss, M. C. & Orenstein, J. in *Millimeter and Submillimeter Wave Spectroscopy of Solids* (ed. Gruener, G.) Ch. 2 (Springer, 1998).
58. Kampfrath, T., Nötzel, J. & Wolf, M. Sampling of broadband terahertz pulses with thick electrooptic crystals. *Appl. Phys. Lett.* **90**, 231113 (2007).
59. Gallot, G. & Grischkowsky, D. Electro-optic detection of terahertz radiation. *J. Opt. Soc. Am. B* **16**, 1204–1212 (1999).
60. Dietze, D., Unterrainer, K. & Darmo, J. Dynamically phase-matched terahertz generation. *Opt. Lett.* **37**, 1047–1049 (2012).
61. Zheng, X., McLaughlin, C., Leahy-Hoppa, M., Sinyukov, A. & Hayden, L. Modeling a broadband terahertz system based on an electro-optic polymer emitter–sensor pair. *J. Opt. Soc. Am. B* **23**, 1338–1347 (2006).
62. Mills, D. L. *Nonlinear Optics: Basic Concepts* (Springer, 1991).
63. Mosendz, O. *et al.* Quantifying spin Hall angles from spin pumping: experiments and theory. *Phys. Rev. Lett.* **104**, 046601 (2010).
64. Freimuth, F., Blügel, S. & Mokrousov, Y. Anisotropic spin Hall effect from first principles. *Phys. Rev. Lett.* **105**, 246602 (2010).